Nano-crystallite bones of *Oreochromis niloticus* and *Katsuwonus pelamis* for the photocatalytic degradation of Congo red dye

Md. Zia Uddin Al Mamun [a],[**], Md. Sahadat Hossain [b],[*], Shyama Prosad Moulick [c],[***], Mohajira Begum [d], Rahima Akter Sathee [a], Md. Sujan Hossen [a], Farhana Jahan [d], Md. Mamunur Rashid [a], Faridul Islam [d], Riyadh Hossen Bhuiyan [e], Md. Sha Alam [f]

[a] Institute of Food Science and Technology (IFST), Bangladesh Council of Scientific and Industrial Research (BCSIR), Dhaka-1205, Bangladesh
[b] Institute of Glass & Ceramic Research and Testing (IGCRT), Bangladesh Council of Scientific and Industrial Research (BCSIR), Dhaka-1205, Bangladesh
[c] BCSIR Laboratories Dhaka, Bangladesh Council of Scientific and Industrial Research (BCSIR), Dhaka-1205, Bangladesh
[d] BCSIR Rajshahi Laboratories, Bangladesh Council of Scientific and Industrial Research (BCSIR), Dhaka-1205, Bangladesh
[e] Fiber and Polymer Research Division, BCSIR Laboratories Dhaka, Bangladesh Council of Scientific and Industrial Research (BCSIR), Dhaka-1205, Bangladesh
[f] Institute of Mining, Mineralogy & Metallurgy (IMMM), Bangladesh Council of Scientific & Industrial Research (BCSIR), Joypurhat-5900, Bangladesh

A R T I C L E   I N F O

A B S T R A C T

The bones of two fish species, *Oreochromis niloticus* and *Katsuwonus pelamis*, were chosen in this research for evaluating their photocatalytic efficacy under solar radiation. The fish bones were isolated and conditioned before analyzing crystallographic parameters. The samples were characterized by using different instrumental techniques such as Fourier Transform Infrared (FTIR), X-ray diffraction (XRD), Energy Dispersive X-ray (EDX), Field Emission Scanning Electronic Microscopy (FESEM), and optical bandgap. From the XRD data, various types of crystallographic information such as crystallite size, microstrain, lattice parameters, dislocation density, degree of crystallinity, crystallinity index, Hydroxylapatite (HAp), the volume fraction of β-TCP, β-Tricalcium phosphate (β-TCP) percentage, and specific surface area were evaluated. Different model equations such as the Sahadat-Scherrer model, Linear Straight-line model, Monshi–Scherrer's method, and Williamson–Hall plot were employed to justify the nano-crystallite size. The photocatalytic efficacy of the two types of samples was explored by changing the catalyst concentration, dye concentration, interaction time, pH of the solution, etc. under solar irradiation.

1. Introduction

There are different types of dyes that are widely used in food, textiles, pharmaceuticals, paper, paint, leather, etc. These dyes are directly or indirectly polluting the environment [1]. The removal of these dyes is essential for a sustainable environment as well as for a

clean water system. During the processing of textile dyes nearly huge amount of water is required (200 L) per Kg of textile production and this large quantity of water produces liquid effluent containing different types of dyes [2,3]. Different types of dyes remain unreacted during the dyeing processes such as reactive dye (20–50%), azo dye (5–10%), sulfur dye (30–40%), direct dye (5–20%), acid dye (7–20%), and pigment dye (1–2%) [4,5]. Most of the synthetic organic dyes are able to produce solution with water and remain unreacted in normal environmental conditions [6]. The textile dyes are very difficult to be degraded under normal wastewater treatment procedures. There are different ways to get rid of the problems associated with polluted water such as adsorption [7], photo-catalyst [8], marine microalgae [9], adsorption on nano composites [10], etc. The photocatalytic way of organic pollutant removal is one of the most used ways and this process produces no secondary pollutants. There are different types of photo-catalysts such as TiO$_2$ [11], g-C$_3$N$_4$/TiO$_2$ [12], TiO$_2$-WO$_3$ Nanocomposite [13], hydroxyapatite [14], ZnCoO [15], ZnFe$_2$O$_4$ [16], ZnO [17], spinel ferrites/metal oxide nanocomposites [18] etc. There remains a cost associated with the catalyst which ultimately enhances the total cost of the wastewater treatment process. To minimize the cost it is necessary to use low-cost catalysts for a sustainable environment [19]. There is a huge demand for water in industries as well as human consumption nearly 4.0 trillion m^3 is required for industrial application and 0.01 trillion m^3/day is demanded by human consumption [20,21]. Thus the cost of the catalyst is an important consideration for the fruitful applications of any catalysis process during waste-water treatment. The source of photon is another issue to be considered during the photocatalyst, normally conditioned light is utilized for this purpose which also demands energy and/or cost [22].

In this research, two types of waste fish bones of the river and marine origin were utilized as the low-cost source of catalysts, and normal sunlight was chosen as the source of photons. The combination of these two low-cost sources was facilitated by the addition of crystallographic analysis of the catalyst to explore the reasons behind the variation of photocatalytic activity.

2. Materials and methods

2.1. Materials

The samples (*Oreochromis niloticus* (Tilapia) and *Katsuwonus pelamis* (Surma)) were received from a local wholesale fish market named Jatrabari, Dhaka, Bangladesh. The samples were kept in an ice box (HDPE ice box, India) with each type of sample in a separate sterile polythene bag to avoid any types of contamination, and then transported (within 1.5 h) to the Fish Technology Research Laboratory of the Institute of Food Science and Technology (IFST), BCSIR, Dhaka. All the chemicals (Congo red dye, NaOH, HNO$_3$) were of analytical grade which were purchased from E-Merck (Darmstadt, Germany), and used exactly as they were received.

2.2. Sample preparation

The collected fish samples were kept in a refrigerator (SJC-328-GY, Sharp, Japan) at −20 °C until further use. The samples were cleaned and de-gutted with a sterile, stainless-steel knife. The cleaned samples were boiled until de-fleshed enough to isolate bones within them. The bones were left for daylong sun drying in non-metal plates with a lid covering the upper side to avoid contamination and then kept in an oven for 1 h at 105 °C. Finally, crushing the dried fish bones into pieces small enough to take into porcelain crucible and sintering it in a muffle furnace at 900 °C for 2 h. The whitish residue remained in the crucible after sintering in the furnace and the samples were packed into zipper bags with proper labeling and stored in a desiccator for further application. To observe the dye degradation capacity, a dye solution (Congo red) of different concentrations (1000, 100, 80, 60, 40, 20, and 10 ppm) has been prepared using deionized water at the required level. All the catalytic activities were performed under the sunlight from December to January.

2.3. X-ray diffraction

A Rigaku SE instrument was engaged to explore the crystallographic information of the natural fish bones of two species. The diffraction data were recorded in the wide range (from 5 to 80°) upholding 0.01 steps. Before analyzing the main sample the instrument was calibrated with the aid of a reference (standard silicon). The instrument temperature was fixed at 20–22 °C for collecting all the data when Copper tube (CuKα, λ = 1.5406 Å) was utilized as the source of X-ray maintaining 50 mA and 40 kV operating current and voltage, respectively.

2.4. FTIR analysis

Fourier transform infrared (FTIR) spectroscopy technique was functionalized to predict the activating groups in the analyzed samples. For the analysis, PerkinElmer Fourier Transformed Infrared Spectrometer was employed which was appended with a diamond attenuated total reflection (ATR) accessory (Frontier, PerkinElmer, UK; Software: Spectrum version 10.4.4). The spectra were recorded with a wavelength range of 650–4000 cm^{-1} at a resolution of 4 cm^{-1}.

2.5. Scanning electron microscopy analysis

To observe the surface morphology and microstructure of the fish bones, field emission scanning electron microscopy (FE-SEM) (model: Zeiss FE-SEM Sigma 300) technique was adopted which was equipped with an EDX facility that helps to unravel the chemical composition of the fish bone samples. The machine was operated at 15 and 20 kV operating voltage.

3. Results and discussion

3.1. Crystallographic analysis

A similar type of X-ray diffraction (XRD) pattern was observed for the two types of fish bones which are visualized in Fig. 1. The XRD data were utilized to estimate the crystallographic parameters of natural apatite. The significant reflection for the Tilapia fish bone was found at d-spacing (in Angström) and the crystallographic plane of 3.42 (002), 3.07 (210), 2.80 (211), 2.77 (112), 2.71(300), 2.62 (202), 2.52 (301), 2.25 (130), 1.94 (222), and 1.83 (213) which were identical to the standard apatite, more precisely hydroxyapatite (HAp) phase according to the standard ICDD database (card no#01-074-0566). Thus, the hexagonal crystal system of the $P6_3/m$ (176) space group was counted for the rest of the calculation to explore different types of crystallographic parameters. A very similar pattern of Surma fish bone was found at d-spacing (in Å) and the crystallographic plane of 3.41 (002), 3.07 (210), 2.80 (211), 2.76 (112), 2.71(300), 2.61 (202), 2.52 (301), 2.25 (130), 1.94 (222), and 1.83 (213). This sample also belongs to the hexagonal crystal system and $P6_3/m$ (176) space group. For both samples, some extra reflection data were noticed which may be due to the existence of a secondary phase of β-tricalcium phosphate (β-TCP). Normally β-TCP is found along with the hydroxyapatite and reflection was counted in ~2.86 (0210) which is characteristic of the β-TCP phase and similar data were documented elsewhere [23].

The crystallographic investigation was accomplished by calculating the crystallite size, lattice parameters, microstrain, dislocation density, crystallinity index, degree of crystallinity, HAp and β-TCP percentage, and volume fraction of β-TCP. To measure these parameters, equations (1)–(10) were taken into consideration and the description of these equations were documented elsewhere [24–26].

$$\text{Crystallite size, } D_c = \frac{K\lambda}{\beta \cos \theta} \tag{1}$$

$$\text{Lattice parameter equation, } \left(\frac{1}{d_{hkl}}\right)^2 = \frac{4}{3}\left(\frac{h^2 + hk + k^2}{a^2}\right) + \frac{l^2}{c^2} \tag{2}$$

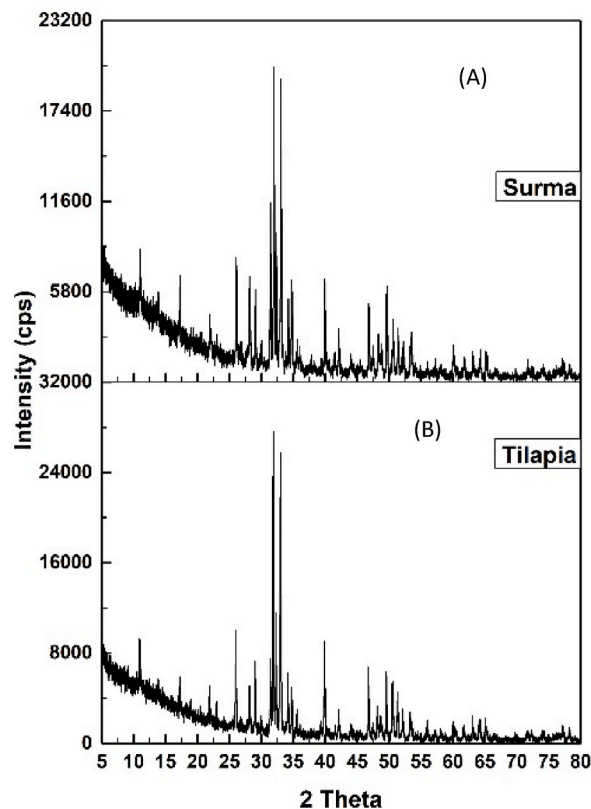$$\text{Microstrain, } \varepsilon = \frac{\beta}{4 \tan \theta} \tag{3}$$

Fig. 1. X-ray diffraction of (A) Surma and (B)Tilapia fish bone.

$$\text{Dislocation density}, \delta = \frac{1}{(D_c)^2} \tag{4}$$

$$\text{Crystallinity index}, CI_{XRD} = \sum \frac{H_{(202)} + H_{(300)} + \big) + H_{(112)}}{H_{(211)}} \tag{5}$$

$$\text{Crystallinity index}, CI_{112/300} = 1 - \frac{V_{112/300}}{I_{300}} \tag{6}$$

$$\text{Degree of Crystallinity}, Xc = \left(\frac{Ka}{\beta}\right)^3 = \left(\frac{0.24}{\beta}\right)^3 \tag{7}$$

$$\text{Percentage of HAp} = \frac{I_{HA(121)}}{I_{HA(211)} + I_{\beta-TCP(0210)}} \tag{8}$$

$$\text{Percentage of } \beta - TCP = \frac{I_{\beta-TCP(0210)}}{I_{HA(211)} + I_{\beta-TCP(0210)}} \tag{9}$$

$$\text{Volume fraction of } \beta - TCP, X_B = \frac{PW_B}{1 + (P-1)W_B} \tag{10}$$

Here, FWHM (full width at half maxima) = β (in radian), K= The Scherrer's constant; θ = diffraction angle (degree); a, b, c and h, k, l are the lattice parameters and Planes of unit cell; Height of the peak of (hkl) plane = $H_{(hkl)}$; K_a = constant for apatite the values 0.24; $I_{\beta-TCP(0210)}$ is the intensity at (0210) plane of β-TCP and $I_{HA(0210)}$ for HAp; W_B = percentage of β-TCP; P = constant = 2.275.

The specific surface area (S) for the two types of samples was counted by fetching equation (11) [27]. In the equation, ρ and D_c symbolize the density and crystallite size of the samples.

$$\text{Specific surface area}, S = \frac{6 \times 10^3}{\rho \times D_c} \tag{11}$$

The characteristics of d-spacing, relative intensities, lattice parameters, and volume of the unit cells are registered in Table 1. And, the crystallite size, lattice parameters, microstrain, dislocation density, crystallinity index, degree of crystallinity, HAp and β-TCP percentage, specific surface area, and volume fraction of β-TCP are recorded in Table 2.

The d-spacing and relative intensities were depicted in Table 1 where lattice parameters along with the unit cell volume were also listed. Lattice parameters of the two types of samples were lower than the standard (International Centre for Diffraction Data) ICDD and resulted in contraction of unit cell volume. The maximum shrinkage was noticed along the a and b axis of the Tilapia fish bone. In tune with the compacting property of the unit cell of the Tilapia fish, a higher microstrain (Table 2) was found for the same sample. For the Surma fish bone, shrinkage occurred along c axis, and a relatively higher unit cell volume was formed but this was also lower than the standard ICDD database.

When the crystallite sizes are small, a larger surface area is found if there is no aggregation among the crystallites or particles. In the case of Tilapia, relatively large crystallite sizes were obtained and thus lower surface area and vice versa have resulted which are registered in Table 2. The larger the crystallite size the probability of generating dislocation is lower, and a similar trend was found for the Tilapia fish bone by forming a lower dislocation density than the Surma fish bone following the sizes of crystallites. For the simplicity of the process, in this case, line dislocation was considered instead of point dislocation, and area dislocation. The dislocations in crystallites are widely known as the crystal imperfection. From the percentages of HAp and β-TCP it was clear that the natural fish bone contained biphasic calcium phosphate (Table 2).

Structural indicators also known as the preference of a certain plane can be estimated from the relative intensities (RI) of XRD data. The relative intensity of (211) plane was considered against (002), (300), and (112) planes which were estimated from Equation (12) [28]. The same standard ICDD card was utilized to compute the standard's relative intensity.

Table 1
Comparison of machine-generated and computed lattice parameters with the standard ICDD data.

Standard values and lattice parameters		Experimental data and the calculated lattice parameters of natural fish bone				Millar index, h k l
ICDD (#01-074-0566)		Tilapia		Surma		
d-spacing (Å)	Intensity, I (%)	d (Å)	I (%)	d (Å)	I (%)	
2.8146	100	2.8070	100	2.8013	100	2 1 1
2.7781	51	2.7711	30	2.7658	35	1 1 2
2.7204	61	2.7132	94	2.7243	88	3 0 0
a = b = 9.424 Å		a = b = 9.399 Å		a = b = 9.437 Å		
c = 6.879 Å		c = 6.856 Å		c = 6.8356 Å		Volume of unit cell, $V = \frac{\sqrt{3}}{2}a^2c$
V = 529.09 Å³		V = 524.52 Å³		V = 527.19 Å³		

Table 2
Crystallographic characterization of Tilapia and Surma fish bone.

Parameter	Tilapia	Surma
Crystallite size, nm	89.9	70
Microstrain, ε	0.078	0.018
Dislocation density, (10^{15} lines/m^2)	0.124	0.20
Crystallinity index, CI_{XRD}	1.52	1.45
Crystallinity index, $CI_{112/300}$	0.94	0.92
Degree of crystallinity	22.59	18.96
HAp percentage (%)	81.78	70.96
β-TCP percentage (%)	18.21	29.03
Volume Fraction of β-TCP	0.34	0.48
Specific surface area, S (m^2/g)	21.25	27.29

$$RI = \frac{I_{(211)}}{I_{(002)} + I_{(112)} + I_{(300)}} \tag{12}$$

The relative intensity of the Tilapia, Surma, and standard were 0.668, 0.602, and 0.677, respectively. The preference growths of the Tilapia and Surma were calculated by exploiting equation (13) [28].

$$\text{Preference growth}, P = \frac{RI - RI_s}{RI_s} \tag{13}$$

The calculated preference growths were −0.0133, and −0.112 for Tilapia and Surma fish bone, respectively. The negative sign in the values represents the thermodynamically unfavorable direction of (211) plane with respect to (002), (112), and (300) planes. Thus, the natural fish bone either marine or river, the (211) plane is not preferable under the experimental conditions.

3.2. FTIR analysis

Fig. 2 represents the Fourier Transform Infrared (FTIR) spectra of Tilapia and Surma fish bone where functional groups were identified from the peaks originating from the vibrational energy of activating groups. The mentioned fish bones contained
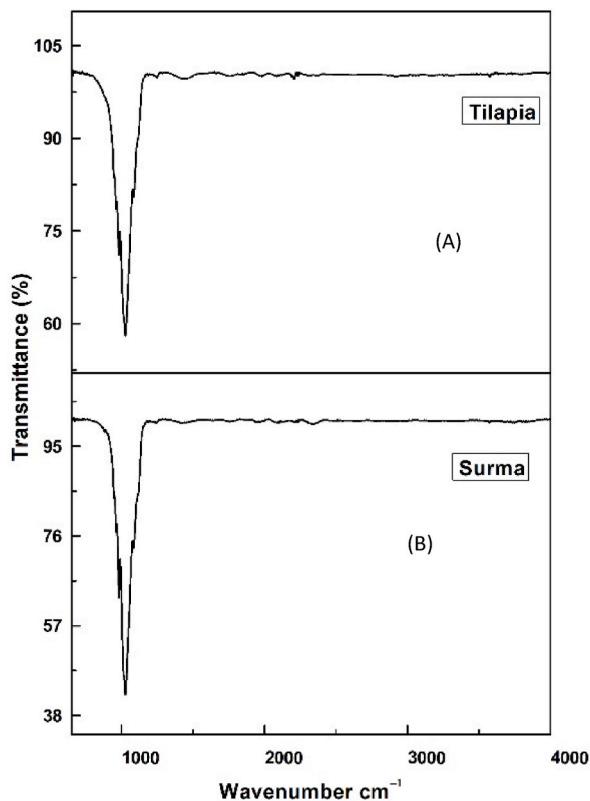

Fig. 2. FTIR spectra of (A) Tilapia and (B) Surma fish bone.

hydroxyapatite as the main constituent comprising the hydroxyl group, phosphate group, and free moisture. The two types of fish bones presented an identical spectrum. The intense peak for the vibration of phosphate groups was revealed at 1027 cm^{-1} and 1029 cm^{-1} for Tilapia and Surma fish bone, respectively. This peak was accompanied by a peak at 982, and 981 cm^{-1} for Tilapia and Surma, respectively. Another peak with more energy was arisen at 1087 and 1089 cm^{-1} for the bone of Tilapia and Surma, respectively. Comparable FTIR data were published in a number of research articles [29]. The higher and lower energy peaks were accountable for the asymmetric stretching vibrational and non-degenerate mode of phosphate group. No significant peak, rather a very small peak, was visualized for the presence of hydroxyl group and free moisture near 3400 cm^{-1}. A very similar types of FTIR spectra were reported in the published literatures [25,30].

3.3. Field Emission Scanning Electronic Microscopy (FESEM)

The surface morphology of Tilapia and Surma fish bone was explored with the aid of FESEM and Energy dispersive X-ray (EDX) which are presented in Fig. 3. A wide variation of the size and shape such as sphere, sponge-like, ribbon-like, niddle shape, and rectangular shape of synthesized hydroxyapatite can be found [31]. But, in the case of natural fish bone, only the sphere shape of particles was noticed no matter whether the origin was river or sea. The particles also remained in the aggregate form with different sizes. EDX analysis was executed to explore the element present in the fishbone. The mass percentages of Tilapia fish bone were 44.05,
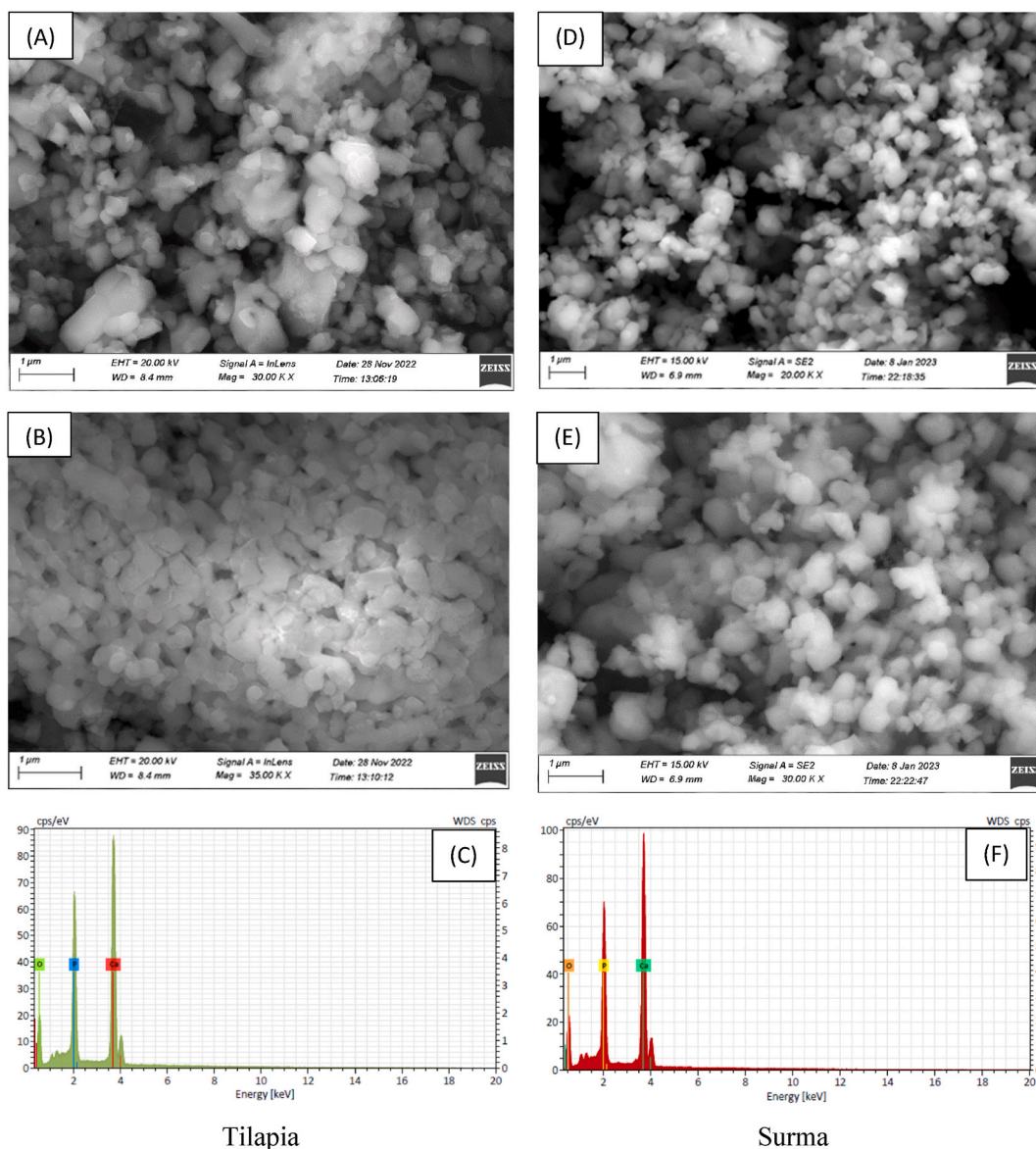

Fig. 3. (A), (B) FESEM of Tilapia and (C) EDX of Tilapia, and (D), (E) FESEM of Surma and (F) EDX of Surma.

11.50, and 44.45 for O, P, and Ca, respectively. Very similar values were found for the Surma fish bone such as 45.05 10.81 44.14 for O, P, and Ca, respectively. The calcium content of the two types of fish bone was also estimated using a flame photometer (LX406FP, LABDEX, UK) where ~30% and ~40% of calcium was found for Tilapia and Surma fish bone, respectively. XRD and FTIR data also presented similar results for the two types of fish bones, and in the case of the FESEM image as well as the elemental analysis by EDX revealed identical results though there was variation in the crystallographic analysis from XRD. Thus, it can be predicted that there was no extra material in the fish bones. Different images were captured for the clarification of data.

3.4. Estimation of crystallite size

3.4.1. Sahadat-Scherrer model

In crystalline materials, the sizes of crystals are very crucial for the fruitful applications of nano-crystallites. Normally, the crystallite sizes are estimated utilizing the Scherrer equation but when the crystal planes are more, then different model equations are employed. To compute crystallite size, Sahadat-Scherrer model was operated for reasonable values and equation (14) represents this model the details can be found elsewhere [26,32]. In this model equation all the reflections were counted for the calculation of crystallite size where a straight line was built which passes through the origin. The formed straight line was compared with the standard equation of the straight line (y = mx), and the crystallite size was estimated by using the slope of the formed equation. Electronic supplementary information (ESI) Figures S_1(A) and S_1(B) represents the graphical form of the Sahadat-Scherrer equation and the inscribed values are for the crystallite size of Tilapia and Surma fish bone.

$$\text{Sahadat} - \text{Scherrer model,} \cos\theta = \frac{K\lambda}{D_{S-S}} \times \frac{1}{FWHM} \tag{14}$$

3.4.2. Linear Straight-line model

The linear Straight-line model is another extensively applied model for the computation of crystallite size which can be formed by rearranging the Scherrer formula. The equation form of the Linear Straight-line model can be expressed as equation (15) the details of this model can be found elsewhere [33].

$$\text{Linear Straight} - \text{line model,} \cos\theta = \frac{K\lambda}{D_c} \times \frac{1}{\beta} = \frac{K\lambda}{D_L} \times \frac{1}{\beta} \tag{15}$$

ESI Figures S_2(A) and S_2(B) visualize the Linear Straight-line model containing the crystallite sizes. The crystallite size obtained from this model were 1733, and 1540 nm for Tilapia and Surma bone, respectively. The crystallite sizes were computed from the slope of equation (15) and compared with the standard equation of a straight line. These crystallite sizes were too large for accepting the values as crystallite size. Thus, this model is not valid for the natural hydroxyapatite of fish bones.

3.4.3. Monshi–Scherrer's method

The Scherrer equation can be rearranged and formed new equation (equation (16)) by taking the logarithm on both sides. The rearranged and logarithm form is commonly familiar with as the Monshi-Scherrer model which can also be utilized to predict the crystallite size and the details of this model are reported elsewhere [34,35].

$$\text{Monshi–Scherrer method,} \ln\beta = \ln\frac{1}{\cos\theta} + \ln\frac{K\lambda}{D_M} \tag{16}$$

The plots were built as presented in ESI Figures S_3(A), and S_3(B) for Tilapia and Surma bone, and using the slope of the build equation the crystallite sizes were measured. Very similar crystallite sizes originated from this method which were very close to the previously mentioned equation and model.

3.4.4. Williamson–Hall plot

Broadening of reflection in XRD depends not only on the crystallite size but also on the intrinsic strain. The Williamson–Hall plot considers the intrinsic strain and thus the formed equations were listed here in equations (17)–(19) for the Uniform deformation model, Stress deformation model, and Energy deformation model, respectively. The details of these models are documented elsewhere [36–39].

The mathematical expression of Uniform Deformation Model (UDM) as:

$$\beta_{\text{total}} \cos\theta = \frac{K_B\lambda}{D_{W-H}} + 4\,\varepsilon\sin\theta \tag{17}$$

The equation form of Uniform Stress Deformation Model (USDM) is:

$$\beta_{\text{total}} \cos\theta = \frac{K_B\lambda}{D_{W-H}} + 4\,\frac{\sigma}{E_{hkl}}\sin\theta \tag{18}$$

The Uniform Deformation Energy Density Model (UDEDM) can be written as:

$$\beta_{\text{total}} \cos \theta = \frac{K_B \lambda}{D_{W-H}} + 4 \left(\frac{2u}{E_{hkl}} \right)^{1/2} \sin \theta \tag{19}$$

The crystallite size of the Tilapia and Surma fish bone estimated from the Williamson–Hall plot are inscribed in the respective figure (ESI Fig. S_4). The crystallite size of the Tilapia fish bone was always higher then Surma bone and the maximum values were found for Tilapia fish bone which cannot be within the acceptable size. Thus, this model fails to fit the two types of fish bone of marine and freshwater.

3.5. Photocatalytic activity

The photocatalytic efficacy of the two types of fish bones was explored by calculating the degradation percentage and degradation capacity as presented in equation 20, and 21, and the details can be found elsewhere [14]. In the equations, the C_o, C_t, V, and W represent the initial concentration, final concentration, volume of aqueous solution, and weight of catalyst, respectively.

$$\text{Degradation percentage}, D_p = \frac{C_o - C_t}{C_o} \times 100 \tag{20}$$

$$\text{Degradation capacity}, q_e = \frac{C_o - C_t}{W} \times V \tag{21}$$

The photocatalytic activity of the fish bones was evaluated under solar radiation between June 2022 to February 2023. The volume of the aqueous solution was 40 mL, the catalyst concentration was 0.1 g, the exposure time was 120 min, and the dye concentration was 20 ppm, if it is not mentioned otherwise.

With the addition of time, the degradation percentage and capacity were augmented and the maximum value was found for the 240 min. The data were collected for 0.1 g, 20 ppm, and 40 mL solution. Fig. 4 visualizes the catalytic effect of Tilapia and Surma fish bone and the time was fixed at 120 min. The Tilapia fish bone revealed a relatively higher degradation percentage and capacity than the Surma fish bone. To explore the catalytic effect, a variation was made in the catalyst amount from 0.1 g to 0.4 g, and the originated plot is illustrated in Fig. 5. With the enhancement of the amount of the catalyst, the degradation percentage was augmented but the degradation capacity was declined. The Tilapia fish bone also exerted a higher degradation percentage than the Surma bone, and a similar trend was noticed for the degradation capacity. A comparison was presented in Table 3 focusing on the degradation of the previous work and the present work. When different dye concentrations were used for 0.1 g catalyst, the degradation percentage was decreased sharply, but the degradation capacity was increased for both types of bone. The degradation percentage and capacity of the Tilapia bone were higher than the Surma bone as found in the previous sections. Fig. 6 shows the effects of dye concentration on the degradation percentage and capacity. The variation of pH in the solution influenced the photocatalytic activity of Congo red dye degradation. The pH varied from 5 to 11 with an interval of two and the data are exerted in Fig. 7. The basic media and acidic media were maintained using ammonium solution and nitric acid, respectively. The maximum degradation was noticed for the neutral pH (pH = 7) and at a lower of higher pH, the degradation was subsided. Another important phenomenon has occurred during the change of pH which is the movement of peak position. At higher pH than the neutral value, the peak position shifting was occurred to the higher wavelength similarly at lower pH the maxima shifted to the lower pH. This movement of the peak position may be due to the bond formation of Congo red dye with the H^+ and/or OH^-.

3.6. Condition of photocatalyst during dye treatment

Fig. 8(A) and (B) represent the FTIR of the Tilapia and Surma fish bone during the catalytic process of dye degradation, the FTIR of
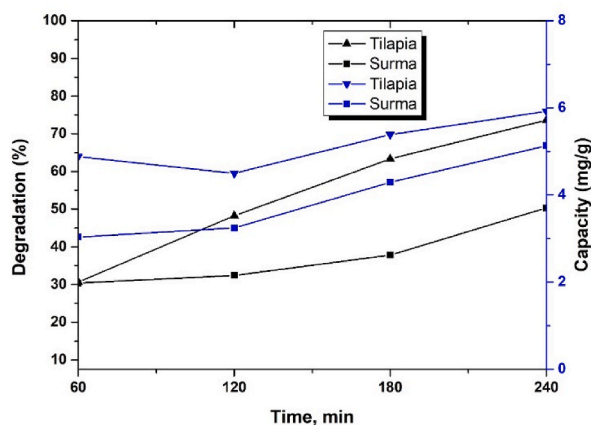

Fig. 4. Optimization of time for 0.1 g catalyst, 40 mL dye solution of 20 ppm.
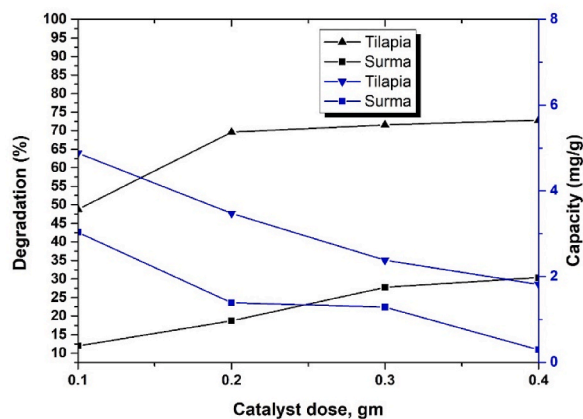
Fig. 5. Optimization of catalyst dose for 120 min time, 40 mL dye solution of 20 ppm.

Table 3
Comparison of the photocatalytic activity of fish bones.

Catalyst/compound	Condition	Degradation (%)/Adsorption capacity	Dye/Pollutant	Ref.
FB-HAp	240 min, 20 ppm, 40 mL, 0.1 g	65%	Congo red	This study
Fish bone powder	4 h, 200 ppm, 300 ppm, 100–700 mg	91–97%	Congo red	[40]
Pretreated fish bone	60 min, pH 10.64, 0.1gL^{-1}	92%	Methyl green	[41]
FB-HAp	75 min, 50 mgL^{-1}, 10 mg	77% (Crystal violet), 87% (Congo red)	Crystal violet, Congo red	[42]
S-HAp (chicken egg shell)	120 min, 10×10^{-6}M, pH 9, 0.2 g	99.82%	Methylene blue	[43]
Ga-HAp (chemically synthesized)	120 min, 1 gL^{-1}, UV light	62%	Methylene blue	[44]
Cu-FB (Fish Bone)	35 min, pH 10, 20 mgL^{-1}, 2 gL^{-1}, 50 °C	98%	Crystal violet	[45]
0.63Cu_HAp	180 min, 20 ppm, 0.1 g	99%	Congo red	[46]
Fish scale chitin	60 min, 30 mgL^{-1}, 2 gL^{-1}, pH 7	95%	Methylene blue	[47]
TiO$_2$/HA/RGO	120 min, xenon lamp irradiation	99.8%	Methylene blue	[48]
HA-MnO$_2$-Chitosan	90 min, UV light (365 nm)	93%	Acid orange 7 (AO7)	[49]
FBBC-800 (fish bone biochar) as persulfate catalyst	60 min, 0.1 gL^{-1}, pH (3.0–9.0)	100%	Phenol	[50]
FB-HAp	20 min, 50 mgL^{-1}, 1 gL^{-1},	49.1 mgg^{-1}	Brilliant green	[51]
Sr–Cu–MnO nanocomposite encapsulated with FB-HAp	–	–	Malachite green and Aniline blue	[52]
CFB-500 (2)	10 min, 100 mgL^{-1}, 250 mg, 30 °C, pH 6.9	>90%	Methylene blue	[53]
HAp-titania (prepared from Cod fish bone)	24 h, 2 ppm, 4 gL^{-1}, UV light	100% (Fluoxetine), 92% (Diclofenac)	Diclofenac, Fluoxetine	[54]

Congo Red Dye was illustrated in Fig. 8(C) the FTIR of pure dye represents the significant peaks at 1638, 2140, and 3340 cm^{-1} wavenumbers on the other hand the pure catalysts showed identical peaks at 982, 1029, and 1089 cm^{-1} (Fig. 2). A similar FTIR spectrum was reported in the literatures with nearly identical peaks [55]. When the catalytic activity of the fish bones was performed, at the initial stage the dye was attached on the surface of the catalyst then the dye was gradually degraded. The intensity of the specific peak (for this case 3340 cm^{-1}) was decreased with the increment of time. A mixture of peaks originated which were the combination peaks of the fish bones and dye together, and this phenomenon was clearly visualized in Fig. 8(D) when the FTIR spectrum was shown in the range of 3000–4000 cm^{-1} wavenumber. With the lapse of time, the intensity of the peak near 3350 cm^{-1} wavenumber was subsided following a pattern which indicated more degradation of dye with time. This experiment was performed for up to 120 min and the mixture of peaks still remained which goes in tune with the photocatalysis activity shown in the previous section. Table 4 represents the FTIR band of the samples.

3.7. Bandgap energy

The optical bandgap energy was calculated for the two types of fish bones which are presented in Fig. 9(A) and 9(B) for Tilapia and Surma, respectively. Equation (15) was employed to compute the direct bandgap and the details are documented elsewhere [24,56,
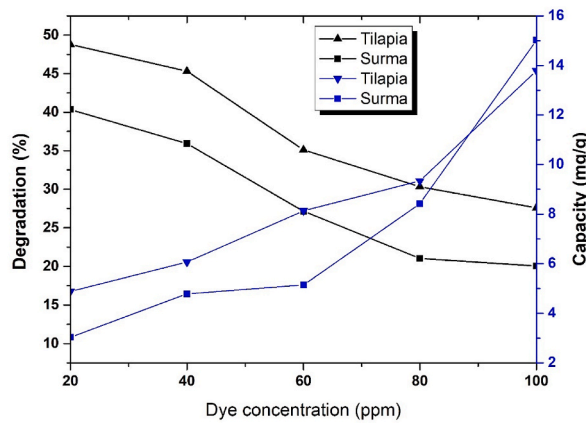
Fig. 6. Optimization of dye concentration for 120 min time, 40 mL dye solution 0.1 g catalyst.
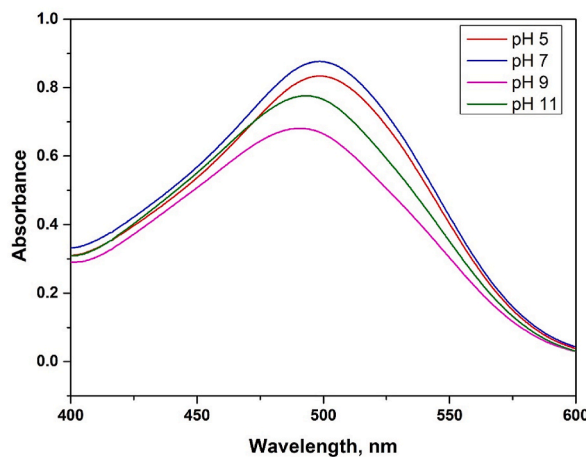

Fig. 7. Effects of pH on the degradation properties.

57].

$$\propto h\vartheta = A\left(h\vartheta - E_g\right)^n \tag{22}$$

Where h is the Plank's constant; ϑ is the photon frequency; $\propto$ is the absorption coefficient; constant value is presented by A; optical band gap energy is denoted by E_g; the value of n is 2 which is characteristic of the direct band gap. For the two types of fish bones, there was no significant change in the optical bandgap energy.

As the optical bandgap of the two types of fish bone was very similar, the variation of the photocatalytic breakdown of Congo Red Dye was not influenced by the bandgap energy. The crystallite size of the Tilapia fish bone was lower than the Surma fish bone which may affect the degradation property of Congo red Dye. There is another important factor to be considered for analyzing more degradation efficacy in the case of Tilapia which is microstrain. The microstrain of the Tilapia is higher than the Surma fish bone. Thus it was assumed that the crystallographic parameters governed the enhance photocatalytic efficiency of Tilapia fish bone than the Surma. The Photocatalytic phenomenon can be explained as presented in equations (16)–(21), a similar type of photocatalytic reaction mechanism was described in the published document [14].
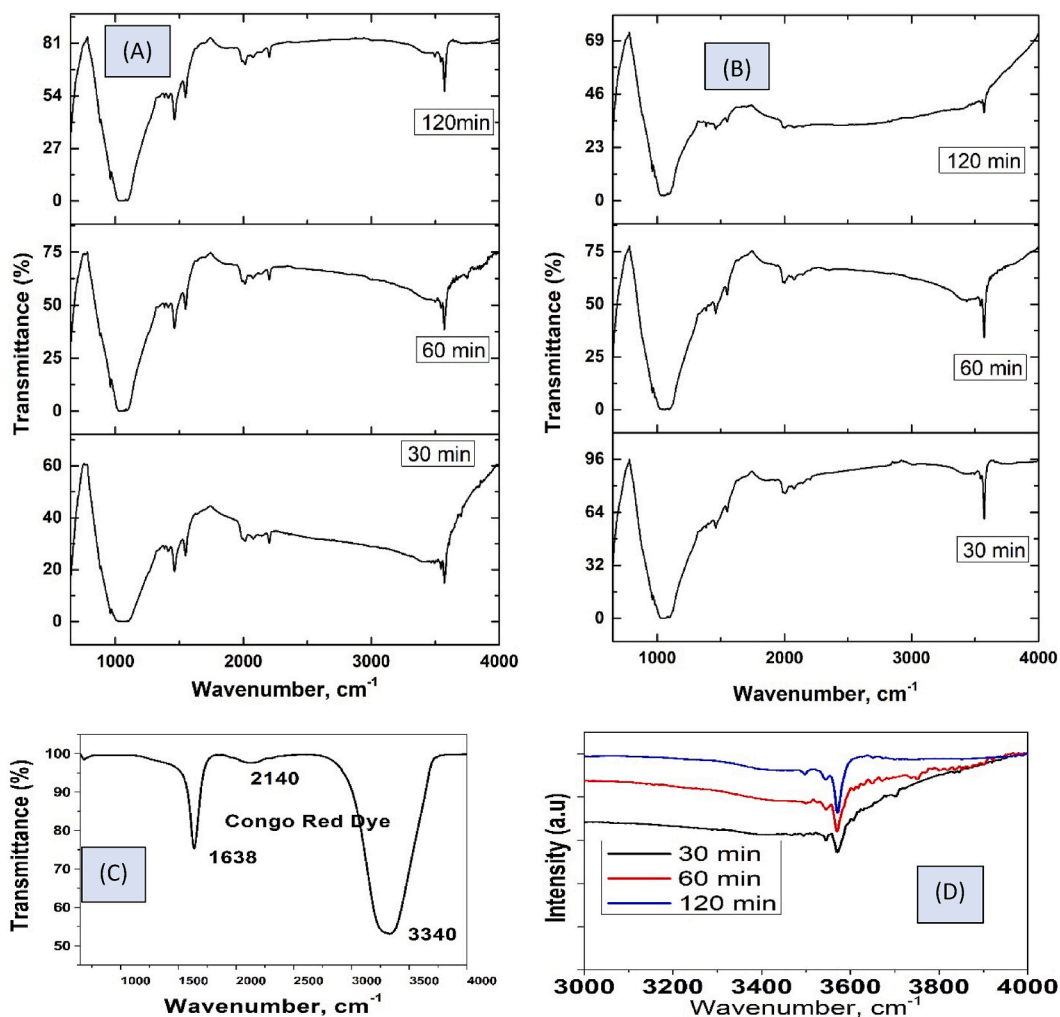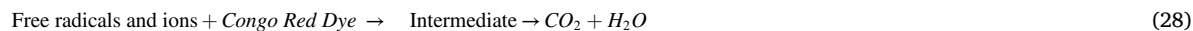
$$\text{Fish bones } \left[\text{Ca}_{10}(\text{PO}_4)_6(\text{OH})_2\right] \xrightarrow{h\vartheta} \text{Ca}_{10}(\text{PO}_4)_6(\text{OH})_2 + h^+ + e^- \tag{23}$$

$$\text{Ca}_{10}(\text{PO}_4)_6(\text{OH})_2 + h^+ + e^- \rightarrow \bullet\text{OH}^\cdot + \bullet\text{OH}^- + \bullet\bullet O_2 \tag{24}$$

$$H_2O + e^- + h^+ \rightarrow \bullet O_2 + OH^- + \bullet\text{OH}^- + H^+ + \bullet O_2^- \tag{25}$$

$$\bullet\text{OH}^\cdot + \bullet\text{OH}^- \rightarrow H_2O_2 \tag{26}$$

Fig. 8. FTIR of dye and catalyst after dye treatment at various time intervals (A)Tilapia, (B) Surma, (C) pure dye, and (D) specific range of FTIR of Tilapia.

Table 4
Band position of the FTIR spectrum of the fish bones and dye.

Band position, cm^{-1}			
Surma	Tilapia	Vibrating bands of fish bones	Dye
982	981	Symmetric stretching vibration (v1)	1638
1027	1029	Stretching vibration (asymmetric) of PO_4^{3-} (v3)	2140
1087	1089	Stretching vibration (asymmetric) of PO_4^{3-} (v3)	3340

$$e^- + h^+ + H_2O_2 \rightarrow \bullet OH^- + \bullet OH^- \tag{27}$$

$$\text{Free radicals and ions} + Congo\ Red\ Dye \rightarrow \text{Intermediate} \rightarrow CO_2 + H_2O \tag{28}$$

4. Conclusion

The waste fish bones were successfully utilized as photocatalysts with the aid of solar irradiation. There remained slight variations among the crystallographic parameters of river and sea fish bones. The river fish presented slightly higher photodegradation than the sea fish bone. Though the photocatalytic efficacy is greatly dependent on the optical bandgap, a very similar bandgap was observed for both types of fish bones. The crystallographic parameters were different and these parameters might influence the higher degradation rate in the case of river fish bones. Nearly, 65% of the Congo Red dye was degraded by the fish bones. Environmental pollution (due to
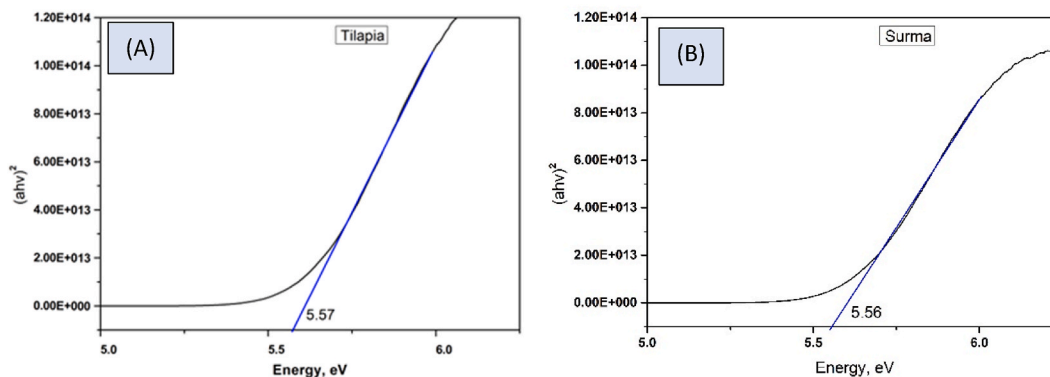
Fig. 9. Optical bandgap energy of the (A) Tilapia and (B) Surma.

organic dye) can be reduced by the fruitful utilization of waste fish bones. Further research can be performed to utilize fish bones to reduce emerging contaminants. It is suggested from this research work that the river fish bone (waste bone) can be utilized to degrade textile effluent in a sustainable way which will minimize the cost of expensive catalysts as well as a source of photons.

Declarations

Author contribution statement

Md. Zia Uddin Al Mamun; Shyama Prosad Moulick: Conceived and designed the experiments, performed the experiments, contributed reagents, materials, analysis tools or data, wrote the paper. Md. Sahadat Hossain: Analyzed and interpreted the data, wrote the paper.

Mohajira Begum: Performed the experiments, contributed reagents, materials, analysis tools or data.Rahima Akter Sathee; Md. Sujan Hossen; Farhana Jahan; Md. Mamunur Rashid; Faridul Islam; Riyad Hossain Bhuiyan; Md. Sha Alam: Performed the experiments.

Data availability statement

Data will be made available on request.

Declaration of competing interest

The authors declare that they have no known competing financial interests or personal relationships that could have appeared to influence the work reported in this paper.

Acknowledgments

Appendix A. Supplementary data

Supplementary data to this article can be found online at https://doi.org/10.1016/j.heliyon.2023.e18012.

References

[1] A.F. Ahamed, N. Kalaivasan, R. Thangaraj, Probing the photocatalytic degradation of acid orange 7 dye with chitosan impregnated hydroxyapatite/manganese dioxide composite, J. Inorg. Organomet. Polym. Mater. (2022) 1–15.
[2] S. Suresh, Treatment of textile dye containing effluents, Curr. Environ. Eng. 1 (2014) 162–184.
[3] A. Munnaf, M.S. Islam, T.R. Tusher, M.H. Kabir, M.A.H. Molla, Investigation of water quality parameters discharged from textile dyeing industries, J. Environ. Sci. Nat. Res. 7 (2014) 257–263.
[4] C.R. Holkar, A.J. Jadhav, D.V. Pinjari, N.M. Mahamuni, A.B. Pandit, A critical review on textile wastewater treatments: possible approaches, J. Environ. Manag. 182 (2016) 351–366.

[5] I. Ilankoon, Y. Ghorbani, M.N. Chong, G. Herath, T. Moyo, J. Petersen, E-waste in the international context–A review of trade flows, regulations, hazards, waste management strategies and technologies for value recovery, Waste Manag. 82 (2018) 258–275.

[6] T. Gulzar, T. Farooq, S. Kiran, I. Ahmad, A. Hameed, Green chemistry in the wet processing of textiles, in: The Impact and Prospects of Green Chemistry for Textile Technology, Elsevier, 2019, pp. 1–20.

[7] Y. Ye, G. Yan, S. Huang, W. Jiang, J. Kang, D. Liu, Y. Ren, B. Xu, J. Zhang, K. Shen, A Feasibility Study of Kitchen Waste and Waste Bentonite as Adsorbent for P-Containing Wastewater Treatment: Performance and Mechanism, Biomass Conversion and Biorefinery, 2023, pp. 1–12.

[8] N. Amir, D. Tahir, H. Heryanto, Synthesis, structural and optical characteristics of Fe3O4/activated carbon photocatalysts to adsorb pesticide waste, J. Mater. Sci. Mater. Electron. 34 (2023) 445.

[9] J. Umamaheswari, R. Rajamanickam, S. Vilvanathan, S. Shanthakumar, K. Venkateswarlu, S. Abinandan, M. Megharaj, Removal of heavy metals and organic pollutants by marine microalgae, in: Marine Organisms: A Solution to Environmental Pollution? Uses in Bioremediation and in Biorefinery, Springer, 2023, pp. 29–64.

[10] S. Asghar, M. Roudgar-Amoli, A. Alizadeh, Z. Shariatinia, Water purification through adsorption of organic pollutant onto novel and effective phosphorus-containing g-C3N4/FeMo0. 5O3 nanocomposites, waterair Soil Poll. 234 (2023) 43.

[11] Y.H. Yoon, S.Y. Lee, J.G. Gwon, E. Vijayakumar, H.G. Lee, W.H. Lee, Enhancement of photocatalytic performance in degradation of aqueous trichloroethylene and methylene blue by using TiO2 thin film fabricated by cellulose nanocrystals templating and Nb doping, Wood Sci. Technol. (2023) 1–19.

[12] S. Li, W. Zhao, D. Xiong, Y. Ye, J. Ma, Y. Gu, g-C3N4/TiO2 uniformly distributed microspheres: preparation for enhanced photocatalytic performance by co-calcination, J. Mater. Sci. Mater. Electron. 34 (2023) 47.

[13] M. Motahari, A. Nourbakhsh, H.R. Bakhsheshi-Rad, N. Lotfian, M. Masoud, A.H. Nourbakhsh, R.D. Dehkordi, K.J. Mackenzie, Photocathodic protection of 316L stainless steel by surface coating of photocatalytic mesoporous TiO2-WO3 nanocomposite, J. Mater. Eng. Perform. (2023) 1–12.

[14] M.S. Hossain, S.M. Tuntun, N.M. Bahadur, S. Ahmed, Enhancement of photocatalytic efficacy by exploiting copper doping in nano-hydroxyapatite for degradation of Congo red dye, RSC Adv. 12 (2022) 34080–34094.

[15] K. Tanji, Y. Fahoul, I. El Mrabet, H. Zaitan, A. Kherbeche, Combined natural mineral@ ZnCoO system for photocatalytic degradation of malachite green under visible radiation, Chem. Afr. (2023) 1–16.

[16] M. Al-Abidy, A. Al-Nayili, Enhancement of photocatalytic activities of ZnFe2O4 composite by incorporating halloysite nanotubes for effective elimination of aqueous organic pollutants, Environ. Monit. Assess. 195 (2023) 190.

[17] P.B. Sreelekshmi, R.R. Pillai, S. Unnimaya, A.L. Anju, A.P. Meera, Biofabrication of novel ZnO nanoparticles for efficient photodegradation of industrial dyes, Clean Technol. Environ. Policy (2023) 1–14.

[18] H. Kumari, S. Chahal, S. Devi, S. Kumar, S. Kumar, P. Kumar, A. Kumar, Spinel ferrites/metal oxide nanocomposites for waste water treatment, Appl. Phys. A 129 (2023) 91.

[19] Z. Wei, C. Xu, B. Li, Application of waste eggshell as low-cost solid catalyst for biodiesel production, Bioresour. Technol. 100 (2009) 2883–2885.

[20] H. Abdulla, M. Zamorano, M.L. Rodríguez, A. El Shahawy, S. Hosny, J. Martín-Pascual, S. El-Shatoury, An overview of agro-food industry wastewater treatment: a bibliometric analysis and literature review, Appl. Water Sci. 13 (2023) 47.

[21] B.P. Walsh, D.O. Cusack, D.T.J. O'Sullivan, An industrial water management value system framework development, Sustain. Prod. Consum. 5 (2016) 82–93.

[22] M.R. Gholipour, C.-T. Dinh, F. Béland, T.-O. Do, Nanocomposite heterojunctions as sunlight-driven photocatalysts for hydrogen production from water splitting, Nanoscale 7 (2015) 8187–8208.

[23] M. Hossain, M. Mahmud, M.B. Mobarak, S. Ahmed, Crystallographic analysis of biphasic hydroxyapatite synthesized by different methods: an appraisal between new and existing models, Chem. Pap. 76 (2022) 1593–1605.

[24] M.S. Hossain, M.A.A. Shaikh, M.S. Rahaman, S. Ahmed, Modification of the crystallographic parameters in a biomaterial employing a series of gamma radiation doses, Mol. Syst. Des. Eng. (2022), https://doi.org/10.1039/D2ME00061J.

[25] MdS. Hossain, MdN. Uddin, S. Sarkar, S. Ahmed, Crystallographic dependency of waste cow bone, hydroxyapatite, and β-tricalcium phosphate for biomedical application, J. Saudi Chem. Soc. 26 (2022) 101559, https://doi.org/10.1016/j.jscs.2022.101559.

[26] MdS. Hossain, M. Mahmud, M.B. Mobarak, S. Sultana, MdA.A. Shaikh, S. Ahmed, New analytical models for precise calculation of crystallite size: application to synthetic hydroxyapatite and natural eggshell crystalline materials, Chem. Pap. (2022), https://doi.org/10.1007/s11696-022-02377-9.

[27] M.S. Hossain, M.N. Uddin, S.A. Jahan, S. Ahmed, Synthesis and characterization of nano crystallite plaster of Paris prepared from waste eggshells and exploration of cytotoxicity, hemolysis and antimicrobial properties, J. Mater. Chem. B 11 (2023) 1057–1067.

[28] M.S. Hossain, S. Ahmed, Synthesis of nano-crystallite gypsum and bassanite from waste Pila globosa shells: crystallographic characterization, RSC Adv. 12 (2022) 25096–25105, https://doi.org/10.1039/D2RA04881Q.

[29] Z. Chen, X. Wang, J. Luo, B. Zhang, F. Shen, B. Li, J. Yang, Synthesis and characterization of rod-like amino acids/nanohydroxyapatite composites to inhibit osteosarcoma, RSC Adv. 12 (2022) 36103–36114.

[30] L. Gritsch, M. Maqbool, V. Mouriño, F.E. Ciraldo, M. Cresswell, P.R. Jackson, C. Lovell, A.R. Boccaccini, Chitosan/hydroxyapatite composite bone tissue engineering scaffolds with dual and decoupled therapeutic ion delivery: copper and strontium, J. Mater. Chem. B 7 (2019) 6109–6124, https://doi.org/10.1039/C9TB00897G.

[31] W.P.S.L. Wijesinghe, M.M.M. G.P, G. Mantilaka, R.M.G. Rajapakse, H.M.T.G.A. Pitawala, T.N. Premachandra, H.M.T.U. Herath, R.P.V.J. Rajapakse, K.G. U. Wijayantha, Urea-assisted synthesis of hydroxyapatite nanorods from naturally occurring impure apatite rocks for biomedical applications, RSC Adv. 7 (2017) 24806–24812, https://doi.org/10.1039/C7RA02166F.

[32] S.M. Tuntun, M.S. Hossain, M.N. Uddin, M.A.A. Shaikh, N.M. Bahadur, S. Ahmed, Crystallographic characterization and application of copper doped hydroxyapatite as a biomaterial, New J. Chem. (2023), https://doi.org/10.1039/D2NJ04130H.

[33] M.S. Hossain, S. Ahmed, Synthesis of nano-crystallite gypsum and bassanite from waste Pila globosa shells: crystallographic characterization, RSC Adv. 12 (2022) 25096–25105.

[34] M.S. Hossain, S.A. Jahan, S. Ahmed, Crystallographic Characterization of Bio-Waste Material Originated CaCO3, Green-Synthesized CaO and Ca (OH) 2, Results in Chemistry, 2023, 100822.

[35] A. Monshi, M.R. Foroughi, M.R. Monshi, Modified Scherrer equation to estimate more accurately nano-crystallite size using XRD, World J. Nano Sci. Eng. 2 (2012) 154–160.

[36] N.T. Tayade, M.P. Tirpude, Frustrated microstructures composite PbS material's size perspective from XRD by variant models of Williamson–Hall plot method, Bull. Mater. Sci. 46 (2023) 20.

[37] D. Jamwal, G. Kaur, P. Raizada, P. Singh, D. Pathak, P. Thakur, Twin-tail surfactant peculiarity in superficial fabrication of semiconductor quantum dots: toward structural, optical, and electrical features, J. Phys. Chem. C 119 (2015) 5062–5073.

[38] A. Velazquez-Palenzuela, F. Centellas, J.A. Garrido, C. Arias, E. Maria Rodriguez, E. Brillas, P.-L. Cabot, Structural properties of unsupported Pt- Ru nanoparticles as anodic catalyst for proton exchange membrane fuel cells, J. Phys. Chem. C 114 (2010) 4399–4407.

[39] G.K. Williamson, W.H. Hall, X-ray line broadening from filed aluminium and wolfram, Acta Metall. 1 (1953) 22–31.

[40] S. Parvin, M.M. Hussain, F. Akter, B.K. Biswas, Removal of Congo red by silver carp (Hypophthalmichthys molitrix) fish bone powder: kinetics, equilibrium, and thermodynamic study, J. Chem. 2021 (2021) 1–11, https://doi.org/10.1155/2021/9535644.

[41] M.A.U.R. Al-Kazragi, D.T. Al-Heetimi, Pretreated fishbone as low cost-adsorbent for cationic dye adsorption from aqueous solutions: equilibrium, optimization, kinetic and thermodynamic study, in: Journal of Physics: Conference Series, IOP Publishing, 2021, 022073, https://doi.org/10.1088/1742-6596/1879/2/022073.

[42] S. Sathiyavimal, S. Vasantharaj, M. Shanmugavel, E. Manikandan, P. Nguyen-Tri, K. Brindhadevi, A. Pugazhendhi, Facile synthesis and characterization of hydroxyapatite from fish bones: photocatalytic degradation of industrial dyes (crystal violet and Congo red), Prog. Org. Coating 148 (2020), 105890, https://doi.org/10.1016/j.porgcoat.2020.105890.

[43] M.B. Mobarak, M.S. Hossain, Z. Yeasmin, M. Mahmud, M.M. Rahman, S. Sultana, S.M. Masum, S. Ahmed, Probing the photocatalytic competency of hydroxyapatite synthesized by solid state and wet chemical precipitation method, J. Mol. Struct. 1252 (2022), 132142, https://doi.org/10.1016/j.molstruc.2021.132142.

[44] R.L. Pereira Rocha, T.L. Silva, F.P. Araujo, E.G. Vieira, L.M. Honório, M.B. Furtini, M.G. da Fonseca, E.C. da Silva-Filho, J.A. Osajima, Gallium-containing hydroxyapatite as a promising material for photocatalytic performance, Minerals 11 (2021) 1347, https://doi.org/10.3390/min11121347.

[45] F. Mejbar, Y. Miyah, A. Lahrichi, S. Ssouni, A. Khalil, L. Nahali, M. Benjelloun, G. El Mouhri, F. Zerrouq, Remarkable CWPO of crystal violet dye removal using the fishbone doped of copper synthesized by impregnation method, Moroc. J. Chem. 9 (2021) 9, https://doi.org/10.48317/IMIST.PRSM/morjchem-v9i3.28836. –3.

[46] M.S. Hossain, S.M. Tuntun, N.M. Bahadur, S. Ahmed, Enhancement of photocatalytic efficacy by exploiting copper doping in nano-hydroxyapatite for degradation of Congo red dye, RSC Adv. 12 (2022) 34080–34094, https://doi.org/10.1039/d2ra06294a.

[47] M.P. Das, M. Renuka, J.V. Vijaylakshmi, P.R. Suguna, Removal of methylene blue by adsorption using fish scale chitin, Nat. Environ. Pollut. Technol. 17 (2018) 993–998.

[48] Q. Yuan, Y. Yang, W. Wu, X. Dai, J. Zhong, Y. Jian, R. Li, T. Wang, H. Yu, X. Xia, Synthesis of a novel TiO2/HA/RGO composite material with photocatalytic activity for dye degradation, Mater. Chem. Phys. 304 (2023), 127847, https://doi.org/10.1016/j.matchemphys.2023.127847.

[49] A.F. Ahamed, N. Kalaivasan, R. Thangaraj, Probing the photocatalytic degradation of acid orange 7 dye with chitosan impregnated hydroxyapatite/manganese dioxide composite, J. Inorg. Organomet. Polym. Mater. 33 (2023) 170–184, https://doi.org/10.1007/s10904-022-02492-w.

[50] X. Ren, J. Wang, J. Yu, B. Song, H. Feng, M. Shen, H. Zhang, J. Zou, G. Zeng, L. Tang, Waste valorization: transforming the fishbone biowaste into biochar as an efficient persulfate catalyst for degradation of organic pollutant, J. Clean. Prod. 291 (2021) 125225, https://doi.org/10.1016/j.jclepro.2020.125225.

[51] Y. Miyah, M. Benjelloun, R. Salim, L. Nahali, F. Mejbar, A. Lahrichi, S. Iaich, F. Zerrouq, Experimental and DFT theoretical study for understanding the adsorption mechanism of toxic dye onto innovative material Fb-HAp based on fishbone powder, J. Mol. Liq. 362 (2022) 119739, https://doi.org/10.1016/j.molliq.2022.119739.

[52] S.D. Roy, K.C. Das, S.S. Dhar, Green Synthesis of Hydroxyapatite Cocooned Nonmagnetic (Sr-Cu-MnO) Nanocomposite for Rapid Degradation of Colored Organic Dyes, Biomass Conversion and Biorefinery, 2023, pp. 1–11, https://doi.org/10.1007/s13399-023-04258-x.

[53] M. Nurhadi, R. Kusumawardani, W. Wirhanuddin, R. Gunawan, H. Nur, Carbon-containing hydroxyapatite obtained from fish bone as low-cost mesoporous material for methylene blue adsorption, Bull. Chem. React. Eng. Catal. 14 (2019) 660–671, https://doi.org/10.9767/bcrec.14.3.5365.660-671.

[54] E.M. Brazón, C. Piccirillo, I.S. Moreira, P.M.L. Castro, Photodegradation of pharmaceutical persistent pollutants using hydroxyapatite-based materials, J. Environ. Manag. 182 (2016) 486–495, https://doi.org/10.1016/j.jenvman.2016.08.005.

[55] P. Mahajan, J. Kaushal, Degradation of Congo red dye in aqueous solution by using phytoremediation potential of chara vulgaris, Chitkara Chem. Rev. 1 (2013) 67–75.

[56] H. Bibi, M. Iqbal, H. Wahab, M. Öztürk, F. Ke, Z. Iqbal, M.I. Khan, S.M. Alghanem, Green synthesis of multifunctional carbon coated copper oxide nanosheets and their photocatalytic and antibacterial activities, Sci. Rep. 11 (2021), 10781, https://doi.org/10.1038/s41598-021-90207-5.

[57] T.H. Le, A.-L. Phan, N. Minh Ty, D. Zhou, J. Qiu, H. Kim Dan, Influences of copper–potassium ion exchange process on the optical bandgaps and spectroscopic properties of Cr 3+/Yb 3+ co-doped in lanthanum aluminosilicate glasses, RSC Adv. 11 (2021) 8917–8926, https://doi.org/10.1039/D0RA10831F.